

# Ultra-efficient magnetism modulation in a Weyl ferromagnet by current-assisted domain wall motion

Qiuyuan Wang<sup>1,11,\*</sup>, Yi Zeng<sup>1,2,\*</sup>, Kai Yuan<sup>1,3</sup>, Qingqi Zeng<sup>4</sup>, Pingfan Gu<sup>1</sup>, Xiaolong Xu<sup>1</sup>, Hanwen Wang<sup>5</sup>, Zheng Han<sup>6,7</sup>, Kentaro Nomura<sup>8</sup>, Wenhong Wang<sup>4,9</sup>, Enke Liu<sup>4,9,§</sup>, Yanglong Hou<sup>2,§</sup>, Yu Ye<sup>1,3,10,§</sup>

<sup>1</sup> State Key Laboratory for Mesoscopic Physics and Frontiers Science Centre for Nano-optoelectronics, School of Physics, Peking University, Beijing 100871, China

<sup>2</sup> Beijing Key Laboratory of Magnetoelectric Materials and Devices, Beijing Innovation Centre for Engineering Science and Advanced Technology, Department of Materials Science and Engineering, College of Engineering, Peking University, Beijing 100871, China

<sup>3</sup> Collaborative Innovation Centre of Quantum Matter, Beijing 100871, China

<sup>4</sup> Beijing National Centre for Condensed Matter Physics and Institute of Physics, Chinese Academy of Sciences, Beijing 100190, China

<sup>5</sup> Shenyang National Laboratory for Materials Science, Institute of Metal Research, Chinese Academy of Sciences, Shenyang 110016, China

<sup>6</sup> State Key Laboratory of Quantum Optics and Quantum Optics Devices, Institute of Opto-Electronics, Shanxi University, Taiyuan 030006, China

<sup>7</sup> Collaborative Innovation Center of Extreme Optics, Shanxi University, Taiyuan 030006, China

<sup>8</sup> Institute for Materials Research and Centre for Spintronics Research Network, Tohoku University, Sendai 980-8577, Japan

<sup>9</sup> Songshan Lake Materials Laboratory, Dongguan 523808, Guangdong, China

<sup>10</sup> Peking University Yangtze Delta Institute of Optoelectronics, Nantong 226010, Jiangsu, China

<sup>11</sup> Department of Electrical Engineering and Computer Science, Massachusetts Institute of Technology, Cambridge, Massachusetts 02139, USA

\* These authors contributed equally.

§ E-mail: [ekliu@iphy.ac.cn](mailto:ekliu@iphy.ac.cn), [hou@pku.edu.cn](mailto:hou@pku.edu.cn), [ye\\_yu@pku.edu.cn](mailto:ye_yu@pku.edu.cn)

**Flexible and efficient manipulation of magnetic configurations can be challenging. In the design of practical devices, achieving high effective magnetic field with low working current is under tight demand. Here, we report a unique method for efficient magnetism modulation by direct current injection in magnetic Weyl semimetal  $\text{Co}_3\text{Sn}_2\text{S}_2$ . We demonstrate that the modulation process stems from current-assisted domain wall motion. Through two independent methods, we reveal that the spin-transfer torque efficiency of  $\text{Co}_3\text{Sn}_2\text{S}_2$  reaches as high as  $2.4\text{-}5.6 \text{ kOe MA}^{-1} \text{ cm}^2$ , and the threshold current density for driving the magnetic domain walls is as low as  $< 5.1 \times 10^5 \text{ A/cm}^2$  without an external field, and  $< 1.5 \times 10^5 \text{ A/cm}^2$  with a moderate external field. Our findings manifest a new and powerful approach for sub-micron magnetism manipulation, and also open the door towards a new paradigm of spintronics that combines magnetism, topology, and metallicity for low-energy consumption memory and computing.**

The interaction between current and magnetic domain wall (DW) is of fundamental interest in spintronics and has inspired a variety of applications in memory and logic devices, such as racetrack memory, to show unprecedented results<sup>1-4</sup>. When a spin-polarized current passes through a non-uniform magnetic texture such as a magnetic DW, spin-transfer torques (STTs) are applied to the local magnetization, so that the magnetic configuration can be directly controlled without the need to use the multilayer film structure required in the spin-orbit torque (SOT) approach<sup>5-13</sup>. But the STT approach also has its own problems. First, the use of STT to push DWs in metallic systems requires a current density threshold of  $10^6$ - $10^8$  A/cm<sup>2</sup> due to the intrinsic and extrinsic pinning effects, which increases the energy consumption of the device and limits its application<sup>14-17</sup>. Although a lower threshold current density can be realized at the cost of a lower DW velocity or a smaller depinning field in a semiconductor<sup>18,19</sup>, an efficient approach that overcomes the magnetic DW pinning to achieve higher DW velocities in metallic systems is under tight demand for practical applications. Second, few attempts have been made to modulate the magnetic properties such as the coercive field in a single material layer utilizing STT, while SOT can be used in some cases when (local) inversion symmetry is broken<sup>20,21</sup>. One reason is that it is challenging to generate non-uniform magnetic textures in a uniformly magnetized sample by STT alone.

The recently discovered magnetic Weyl semimetal  $\text{Co}_3\text{Sn}_2\text{S}_2$  combines topology, magnetism, and metallicity in a single material, making it a promising platform for studying current-controlled magnetism manipulation. Theoretically, the linear dispersion of Weyl fermions significantly alters the form of STT, leading to a large non-adiabatic torque and ensuring that the adiabatic torque vanishes at the lowest order of the axial magnetic field<sup>22,23</sup> (see Supplementary Note 1 for details). Since the non-adiabatic STT-driven DWs are less affected by the intrinsic pinning effect, a lower intrinsic current threshold and a higher DW motion efficiency are anticipated in  $\text{Co}_3\text{Sn}_2\text{S}_2$ , but relevant experiments are still lacking.

We report that in the synthesized  $\text{Co}_3\text{Sn}_2\text{S}_2$  flakes (35-165 nm thick, grown on sapphire or  $\text{SiO}_2$  substrates), a low current density on the order of  $10^5$ - $10^7$  A/cm<sup>2</sup> can reduce the coercive field  $H_C$  of  $\text{Co}_3\text{Sn}_2\text{S}_2$  from as high as 20 kOe down to smaller than 0.1 kOe. The threshold current to reduce  $H_C$  as well as the symmetry of the  $\pm$  current can be further tuned by the geometry of the contact electrode. We reasonably deduce that the magnetism modulation behavior mainly comes from the current-assisted DW motion, specifically, through STT. To evaluate the STT efficiency, we fabricated  $\text{Co}_3\text{Sn}_2\text{S}_2$  nanowire devices and measured their DW velocities in the parameter space of current, magnetic field, and temperature. We find a giant STT effective field of 2.4-5.6 kOe MA<sup>-1</sup> cm<sup>2</sup> at 150 K, which is even larger at lower temperatures, consistent with the results obtained by the reduction of coercive field in Hall devices. Also, very low current-induced DW motion thresholds of  $< 5.1 \times 10^5$  A/cm<sup>2</sup> (without external field) and  $< 1.5 \times 10^5$  A/cm<sup>2</sup> (with modest external field) in  $\text{Co}_3\text{Sn}_2\text{S}_2$  are obtained. These findings demonstrate the high efficiency of the current-assisted DW motion and thus magnetism modulation in  $\text{Co}_3\text{Sn}_2\text{S}_2$ . Similar characteristics of other room-temperature magnetic Weyl semimetals are thus of great interest for broader applications<sup>24,25</sup>.

### **Magnetism modulation with ultra-high efficiency in $\text{Co}_3\text{Sn}_2\text{S}_2$**

$\text{Co}_3\text{Sn}_2\text{S}_2$  is a ferromagnetic Weyl semimetal with a quasi-2D crystal structure consisting of stacked kagome lattices of cobalt atoms (Fig. 1a) and three pairs of Weyl points that are  $\sim 50$  meV above the Fermi level in the first Brillouin zone<sup>26-29</sup>. In our work, high-quality single-

crystalline  $\text{Co}_3\text{Sn}_2\text{S}_2$  nanoflakes were directly grown on substrates (sapphire or  $\text{SiO}_2$ ) via a modified chemical vapor transport method and then fabricated into standard Hall-bar devices (Fig. 1b, see details in Fig. S1 and Methods). From the electrical transport measurements, the  $\text{Co}_3\text{Sn}_2\text{S}_2$  nanoflake shows ferromagnetism with a Curie temperature of about 175 K (Fig. 1c) and a large anomalous Hall angle up to 25.0%, consistent with those of reported bulk  $\text{Co}_3\text{Sn}_2\text{S}_2$  single crystals<sup>26,27,30</sup>.

The magnetization of  $\text{Co}_3\text{Sn}_2\text{S}_2$  lies perpendicular to the sample plane. Due to the kagome lattice structure and the quasi-2D electronic and magnetic characteristics,  $\text{Co}_3\text{Sn}_2\text{S}_2$  exhibits a relatively small saturation magnetization  $M_S$  of 29.3-48.8  $\text{emu}/\text{cm}^3$  as an itinerant ferromagnet, but an extremely large out-of-plane anisotropy field  $H_K$  of 80-118 kOe at 150-170 K (the temperature range of this paper's main focus), which is much larger than the coercive field  $H_C$  of no larger than 4 kOe in this temperature range<sup>31</sup>. The corresponding magnetic anisotropy constant  $K$  in this temperature range is  $(1.17\text{-}2.88) \times 10^6 \text{ erg}/\text{cm}^3$  (full description of electrical and magnetic properties in Supplementary Note 3). In both SOT and STT cases, small magnetization will result in high current-induced torque efficiency, which is expected to be inversely proportional to the free layer magnetization. For example, in the flow (i.e. linear) region, the current-induced DW velocity is  $v_{\text{DW}} \propto PJ/M_S$  ( $P$ , the spin polarization of the current;  $J$ , the current density), regardless of whether adiabatic or non-adiabatic STT is considered. Meanwhile, the field-driven DW velocity is  $v_{\text{DW}} \propto \Delta = (A/K)^{1/2}$  ( $\Delta$ , magnetic DW width constant;  $A$ , exchange stiffness). In other words, the large magnetic anisotropy will not only form thinner DWs, allowing downscaling of spintronic devices, but also reduce the perturbation from external fields, improve device stability, and further increase the current-induced effective field<sup>32-34</sup>.

To explore the significant current-induced effects in  $\text{Co}_3\text{Sn}_2\text{S}_2$ , we measured the anomalous Hall resistance,  $R_{\text{yx}}$ , hysteresis loops of the Hall devices under different DC currents. Surprisingly, in this simple device structure containing only one material –  $\text{Co}_3\text{Sn}_2\text{S}_2$  and Cr/Au contacts, a clear current modulation pattern of the hysteresis loop is observed (Fig. 1d and Fig. 1e from device 1). When the applied DC current is lower than the threshold current, the hysteresis loop and coercive field remain roughly unaffected – they only change slowly following the temperature rise caused by Joule heating. But when the current exceeds the threshold, the coercivity begins to drop rapidly, and eventually reaches a remarkably small value as the current increases. The change of  $H_C$  in this region deviates significantly from the change caused by pure thermal effect (Fig. 1d). The current threshold behaviors are observed at all measured temperatures from 5 K to 150 K (more data is provided in Supplementary Fig. S3). Eight samples from three different growth batches are tested, and all samples show the same current modulation behavior. These devices have a thickness of 35-165 nm, a width of 4-6  $\mu\text{m}$ , and a length of 10-40  $\mu\text{m}$ , and they are grown and fabricated on sapphire or  $\text{SiO}_2$  substrates, demonstrating the robustness of this phenomenon. At 5 K, the coercive field does not decrease to the lowest value (Fig. 1d) because we limit the maximum applied current to 5.4 mA to protect the device for subsequent measurements. In another device,  $H_C$  up to 20 kOe is tuned to  $< 0.1$  kOe by current (Supplementary Fig. S4). Noticeably, if we define the efficiency of the current-induced magnetism modulation effect as the slope  $\Delta H_C/\Delta j$  in the region above the threshold (thermal effect contribution is subtracted, see detailed discussion of thermal effect in Supplementary Note 5), it reaches 3.1 kOe  $\text{MA}^{-1} \text{cm}^2$  (150 K) - 10.4 kOe  $\text{MA}^{-1} \text{cm}^2$  (50 K).

For comparison, the effective field generated by SOT in BiSb/MnGa ( $\theta_{\text{SH}} \approx 52$ ) is 2.3 kOe  $\text{MA}^{-1} \text{cm}^2$ , while the reported STT efficiency of driving magnetic DWs is 0.4 kOe  $\text{MA}^{-1} \text{cm}^2$  in (Ga,Mn)(As,P) and only 0.2-8.0 Oe  $\text{MA}^{-1} \text{cm}^2$  in Co-Pt-based systems<sup>12,35,36</sup>.

### Current-assisted domain wall motion model

The giant efficiency of current-induced  $H_C$  reduction is unusual. To unravel the underlying mechanism, we first investigated the magnetization reversal nature of the  $\text{Co}_3\text{Sn}_2\text{S}_2$  samples. Figure 2a shows the hysteresis loop evolution as a function of the field angle in the  $xz$ -plane.  $H_C$  increases monotonically with  $\theta$  and follows the standard  $1/\cos\theta$  behavior (Fig. 2b), indicating that the magnetization reversal process in  $\text{Co}_3\text{Sn}_2\text{S}_2$  is dominated by DW motion rather than coherent rotation<sup>37,38</sup>. The multi-domain nature of the switching is also evidenced by the fact that  $H_C \ll H_K$  (Fig. S2d). As a result, any macro-spin model fails. Meantime, all hysteresis loops are rectangle-shaped, clarifying that the mobile DWs suddenly appear at  $H_C$  (nucleation) and then continue to move (propagation) until the magnetization of the whole sample is reversed.

Next, devices with asymmetric contact electrodes (devices 2 and 3) were fabricated to explore how current affects the DW nucleation and propagation. Figure 2c shows the representative hysteresis loops of device 2 under different currents, and Fig. 2d plots the variation of  $H_C$  with the current. In this device, several characteristic features imply that the DW nucleation process is greatly modified by DC current injection, therefore the magnetic hysteresis loops and  $H_C$  are modulated. First, under the small current when  $H_C$  begins to decrease, the hysteresis loop remains rectangular ( $-7.6$  mA in Fig. 2c) and shrinks with the current, indicating that the coercive field  $H_C$  is still determined by the nucleation field  $H_n$ . Under larger currents, the hysteresis loop becomes irregular, and the sample enters a multi-domain state ( $-11.1$  mA and  $4.6$  mA in Fig. 2c). In this region,  $H_n$  is the field when the total magnetization starts to drop, while DW propagation determines the field that fully reverses the sample. As shown in Fig. 2c, both the nucleation and propagation fields are reduced by large currents. Second, an abnormal increase of  $H_C$  with the increase of the current absolute value occurs between  $-(0.9-1.7)$  mA. Marked by the red dashed line in Fig. 2d, starting at the same magnitude of the positive current threshold  $|I_{C,1}^+| = |I_{C,1}^-| = 0.9$  mA,  $H_C$  decreases with  $|I_{C,1}^+|$ ,

but increases with  $|I_{C,1}^-|$ , which shows that  $\Delta|H_C| = \Delta|H_n|$  is an odd function of current. This symmetry is different from the common current effects in perpendicularly magnetized samples (details in Supplementary Note 6), including Joule heating (even function of current, regardless of homogenous or nonhomogeneous cases), SOT (even function of current when the external field is out-of-plane) and Oersted field (odd function of the field)<sup>39,40</sup>. There must be some other responsible effects, which we will attribute to the current-assisted DW motion that altered the DW nucleation process discussed later in this paper. Third, the appearance of another platform of  $H_C$  and a larger negative current threshold  $I_{C,2}^- \approx -6.2$  mA (the blue dashed line in Fig. 2d) indicates that multiple nucleation sites are involved, otherwise this non-monotonic change on the negative current side will not occur.

To further study the contributive nucleation location of DW and clarify its STT origin, we designed a device (device 3) with two drain electrodes of different shapes and contact areas (Fig. 2e). When current is injected through paths 1-2 or 1-3, the path with the smaller electrode

2 shows an evidently smaller positive current threshold than that of electrode 3, while the negative current thresholds of the two paths are almost the same (Fig. 2f). This signifies that the effective nucleation of DW is close to the source or drain electrodes – the negative current only contributes to the DW nucleation near electrode 1, while the positive current only contributes to the DW nucleation near electrode 2 or 3. The local and unidirectional nature of this interaction further suggests the STT origin of this phenomenon. Besides, the unidirectionality confirms that the direction of the current-induced force on magnetic DWs is along the electron flow direction (consistent with the DW velocity measurement results discussed later), and demonstrates that the current modulation behavior can be artificially controlled by the design of the electrode geometry.

Now we can use the current-assisted DW motion model to describe all the observed magnetism modulation phenomena (Fig. 2g). As mentioned earlier, under a moderate current, the coercive field  $H_C$  of the sample is determined by the nucleation field  $H_n$ . Note that there can be multiple nucleation sites, and  $H_C$  equals the lowest nucleation field, that is,  $H_C = H_{n, \min}$ . From the above experiments, the current will affect the DW nucleation process near the source and drain electrodes. We assume that the injected current applies STT on the DW. Since the force induced by STT is an odd function of current, its influence on  $H_n$  depends on the current direction. Since the magnetization easy-axis is out-of-plane and perpendicular to the current, the magnetization direction will not affect  $H_n$ . For a specific nucleation location,  $H_n$  decreases (increases) when the current induced force is along (against) the DW propagation direction. Figure 2g illustrates how the DC current affects the DW nucleation process at two different locations with opposite DW propagation directions. The blue and red lines represent the  $H_n$  at the two locations, whose nucleation fields and current thresholds are slightly different. Then, the coercive field  $H_C$  is represented by the solid lines, which is determined by the minimum  $H_n$  values under different applied currents. We found that this simple model captured the two main abnormal features we observed experimentally in Fig. 2d. First, the decisive nucleation position is switched at  $H_{n,1} = H_{n,2}$  (marked by the purple arrows in Fig. 2d and Fig. 2g), resulting in asymmetric threshold currents of  $I_{C,1}^+ \approx 1.2$  mA and  $I_{C,2}^- \approx -6.2$  mA. Second,  $H_C$  increases abnormally with the current at  $I_{C,1}^-$  (symmetric to  $I_{C,1}^+$ ), as expected in this current-assisted DW motion picture. This model is further verified by the control experiments illustrated in Fig. 3c-h, and a detailed discussion of the effect of current on nucleation can be found in the Supplementary Information Note 6 and 8.

### **Domain wall velocity measurement revealing giant STT efficiency**

Despite the above model qualitatively explains the magnetism modulation phenomenon, it lacks a quantitative measurement of DW dynamics. To better assign the current-assisted DW motion model and understand its ultra-high efficiency, we managed to measure the field and current dependent DW velocity in  $\text{Co}_3\text{Sn}_2\text{S}_2$  through the time-of-flight method<sup>41,42</sup>. The measurement scheme is depicted in Fig. 3a. We fabricated a 1  $\mu\text{m}$  wide and 62 nm thick  $\text{Co}_3\text{Sn}_2\text{S}_2$  nanowire with three pairs of Hall bars in the middle, two Au heaters on both sides, and source/drain electrodes (device 4). The sample magnetization is first saturated by a negative field larger than  $H_C$ . Next, the field is changed to positive  $H_z < H_C$ , and a DC current  $I_{DC}$  is applied in the nanowire. At this time, the sample is magnetized in the  $-z$ -direction. The magnetic DW is then prepared by injecting a current pulse into the heater (the left one in the schematic). Under the mutual effect of current, field and heating, a DW is generated near the

heater and propagates in the opposite direction of  $I_{DC}$  (from left to right in the schematic). The motion of the DW is monitored by an oscilloscope recording the Hall voltage change (thus the change of  $R_{yx}$ ) on two Hall bars separated by  $15\ \mu\text{m}$ , so that the DW velocity can be obtained as a function of  $H_z$  or  $I_{DC}$ . The typical waveforms of the heater pulse and  $R_{yx}$  changes are shown in Fig. 3b. Clearly, the DW propagates across Hall bar 2 and 3 subsequently (along with the direction of the electron flow), resulting in a  $2R_0$  change in  $R_{yx}$ , where  $R_0$  is the saturated anomalous Hall resistance. We also used a lock-in amplifier to monitor the  $R_{yx}$  at Hall bar 1 to ensure the magnetization direction and saturation of the nanowire before and after the current pulse.

Before the DW dynamics measurement, we utilized the nanowire device to cross-check the role of Joule heating and current-assisted DW motion by STT in the magnetism modulation process (Fig. 3c-h). A tiny  $1\ \mu\text{A}$  AC current is used to track the Hall resistance  $R_{yx}$ , while the effects of Joule heating and STT are separated by the DC current injection into the heater and  $\text{Co}_3\text{Sn}_2\text{S}_2$  nanowire, respectively. Figures 3c-d show the  $R_{yx}$  hysteresis loops as a function of the heater current  $I_{\text{heater}}$  from the configuration that current is only applied on the heater. When  $I_{\text{heater}}$  is large enough, the temperature near the heater will rise, lowering the energy barrier for DW nucleation, so  $H_C$  will decrease. Because it is a pure thermal effect, negative  $I_{\text{heater}}$  also has the same effect (not shown in the figure). In addition,  $I_{\text{heater}}$  will not increase  $H_C$ . Figures 3e-f show the results when both the heater and the nanowire run current.  $I_{\text{heater}}$  is now fixed at  $15\ \text{mA}$  to release the magnetic DW near the heater and let it propagate from left to right during the magnetic reversal process. The resulting hysteresis loops as a function of the current in the nanowire  $I_{sd}$  (positive direction defined from right to left) are shown in Fig. 3f. Contrary to the heater-only case (Fig. 3d),  $\pm I_{sd}$  show opposite modulation behavior to  $H_C$ . Positive  $I_{sd}$  exerts a force on the DW away from the heater to help its nucleation and propagation process, thus reducing  $H_C$ , and vice versa. In the intermediate current region between  $-0.2\ \text{mA}$  and  $0\ \text{mA}$ , the modulation efficiency  $\Delta H_C/\Delta J$  reaches  $2.2\ \text{kOe MA}^{-1}\ \text{cm}^2$ , very close to the value obtained in device 1. In Fig. 3g-h, when only  $I_{sd}$  is applied, the hysteresis loop remains unchanged in the same  $I_{sd}$  range as in Fig. 3e-f, indicating that  $I_{sd}$  does not bring severe heating effect. The comparison of the three cases in Fig. 3c-h illustrates that STT plays an important role in the magnetism modulation process by affecting DW nucleation, thus resulting in the ultra-high efficiency, while Joule heating ensures that the dominated nucleation process occurs near the source/drain electrodes, so DW propagates unidirectionally during the magnetization reversal process and  $H_n$  can be effectively modulated.

We finally perform DW velocity measurements to give an unambiguous result of STT efficiency. Figure 3i shows the contour plot of the DW velocity  $v_{DW}$  as a function of  $H_z$  and  $J$ , where three ‘‘iso-speed’’ lines with an interval of  $1\ \text{m/s}$  are displayed by the black dashed lines. Interestingly,  $v_{DW}$  shows an excellent linear dependence on the field and current density covering our whole measurement range, which can be expressed as  $v_{DW} = \eta J + \mu H_z$ , where  $\eta$  and  $\mu$  are the current- and field-dependent domain wall mobility, respectively. The linear relationship can be seen more clearly in Fig. 3j,k, where the dependence of  $v_{DW}$  on  $J$  and  $H_z$  is measured at various temperatures, showing that the magnetic DW enters the linear flow region under a small current density of  $\sim 10^5\ \text{A/cm}^2$  and magnetic field of  $\sim 0.1\ \text{kOe}$ <sup>32</sup>. The linear relationship demonstrates the field-like effect of STT on DW dynamics, so the effective field of STT can be obtained as  $\eta/\mu$ , reaching  $2.4\ \text{kOe MA}^{-1}\ \text{cm}^2$  at  $150\ \text{K}$  in device 4, and  $5.6\ \text{kOe}$

$\text{MA}^{-1} \text{cm}^2$  in another device (device 5, Supplementary Fig. S9). Note that the magnetism modulation efficiencies observed in devices 1-3 at the same temperature are 3.3-3.8 kOe  $\text{MA}^{-1} \text{cm}^2$ , which is within the STT efficiency range obtained by DW dynamics measurements. A full comparison between these two efficiencies obtained from different devices is depicted in Fig. 4. Their values and the temperature-dependences are well matched (see Supplementary Note 8), which strengthens the current-assisted DW motion model and provides direct evidence of the ultra-high STT efficiency in  $\text{Co}_3\text{Sn}_2\text{S}_2$ .

Another crucial parameter in DW dynamics is the threshold current density  $J_c$ , above which the current-induced DW motion can be achieved. In our experiments, even the lowest applied current density exceeds the threshold because a finite magnetic field and current are required to nucleate the DW and generate observable electrical signals. As a result, only the upper bound of  $J_c$  can be given. We further calculate an effective actual threshold value  $J_c^* = J_c + (\mu/\eta) H_z$ , which is ensured by the field-like effect of the current. From Fig. 3j, we see that  $J_c < 1.6 \times 10^5 \text{ A/cm}^2$  under 0.2 kOe field, giving  $J_c^* < 2.8 \times 10^5 \text{ A/cm}^2$  at 167.5 K. A lower threshold is observed in device 5, with  $J_c < 1.0 \times 10^5 \text{ A/cm}^2$  under 0.2 kOe field and  $J_c^* < 1.5 \times 10^5 \text{ A/cm}^2$  at 160 K. In addition, DW nucleation is occasionally achieved without magnetic field in this device. Therefore, we obtain the maximum upper bound of  $J_c < 5.1 \times 10^5 \text{ A/cm}^2$  at 160 K (Supplementary Fig. S9), on the same order of magnitude as  $J_c^*$ , which is still two orders of magnitude smaller than the value of common metallic ferromagnets.

## Discussion

In conclusion, we find that DC current significantly modulates the coercivity and thus magnetization reversal process in  $\text{Co}_3\text{Sn}_2\text{S}_2$  nanoflakes with ultra-high efficiency. The mechanism is carefully studied and confirmed to be the current-assisted DW motion enabled by the giant STT efficiency in  $\text{Co}_3\text{Sn}_2\text{S}_2$ . The low threshold current density and the pure field-like effect of the current to drive the DWs coincides with microscopic spin-torque theory based on Weyl fermions – the topological band structure could lead to anomalous coupling between magnetism and transport, thereby greatly modifying the form of spin torques<sup>22,23</sup>. It may explain why similar current modulation behavior has never been observed in conventional materials before. This work provides a new scheme of magnetism manipulation, demonstrates that STT in metallic systems can produce a large effective field comparable to the best results of SOT, and sheds light on the yet juvenile study of DW dynamics in magnetic Weyl semimetals<sup>43,44</sup>. Direct control of magnetism by current injection into a single material with large perpendicular magnetic anisotropy may enable more flexible design on DW functional devices, which are more compact, stable, and power-saving. In addition, DW velocity in a larger range of current density is highly anticipated to better study the current threshold, Walker breakdown, and the non-adiabatic STT parameter  $\beta$  in the magnetic Weyl semimetals.

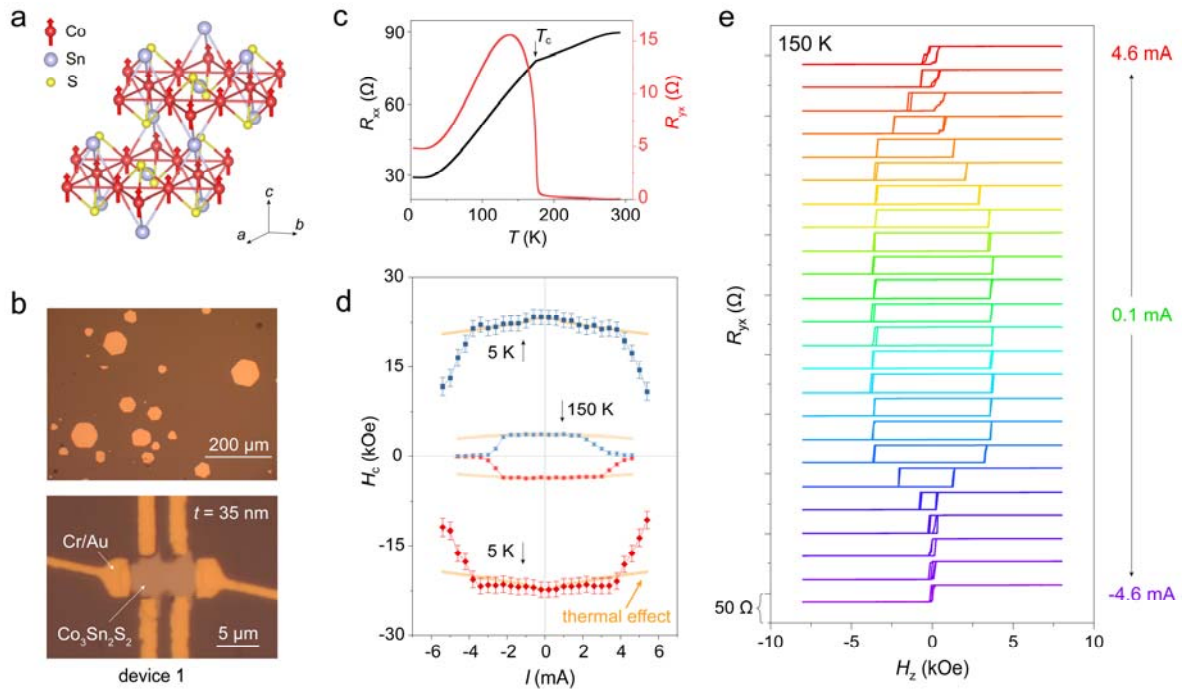


**Fig. 1 Current modulation of the reversal process.** **a**, Crystal structure of  $\text{Co}_3\text{Sn}_2\text{S}_2$  with a space group of  $R\bar{3}m$  (no. 166). The cobalt atoms form a quasi-2D kagome lattice. **b**, Optical images of the as-grown  $\text{Co}_3\text{Sn}_2\text{S}_2$  nanoflakes on a sapphire substrate and a fabricated 35 nm thick Hall-bar device (device 1). **c**, The temperature dependence of the longitudinal ( $R_{xx}$ ) and transverse ( $R_{yx}$ ) resistance under 0.1 kOe field cooling along the  $c$ -axis. A Curie temperature of  $T_C \approx 175$  K is obtained. **d**, When the applied DC current exceeds the threshold, the coercive field  $H_C$  (red and blue points) begins to decrease rapidly, showing significant discrepancy from the pure thermal effect (orange lines, obtained by using the value of  $R_{yx}$  as an internal thermometer). **e**, The hysteresis loops of  $R_{yx}$  under different DC currents measured at 150 K. Each loop is measured twice to ensure repeatability.



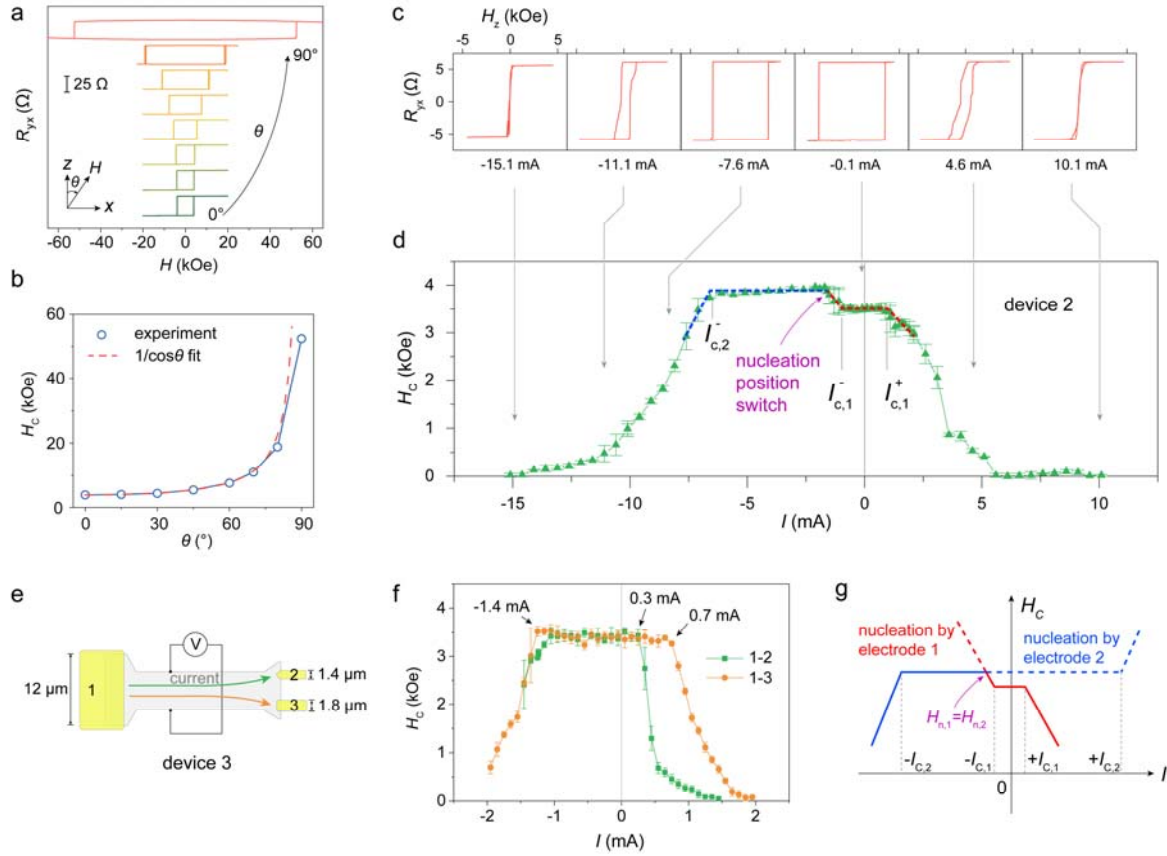


**Fig. 2 Current-assisted domain wall motion model.** **a**, Field angle dependence of  $R_{yx}(H)$ . The sample lies in the  $xy$ -plane. Magnetic field  $H$  is applied in the  $xz$ -plane, and  $\theta$  is the angle between  $H$  and the  $z$ -axis. **b**, Coercive field  $H_C$  as a function of  $\theta$ . Error bars (both horizontal and vertical) are smaller than data points. The red dashed line represents  $H_C(\theta=0)/\cos\theta$ , the predicted value when the magnetization reversal process is dominated by DW motion. **c-d**,  $H_C$  and representative hysteresis loops of device 2 ( $40\ \mu\text{m}\times 6\ \mu\text{m}\times 92\ \text{nm}$ ) under different DC currents, showing features including the abnormal increase of  $H_C$ , asymmetric current thresholds, and multi-domain. **e**, Schematic of device 3 ( $25\ \mu\text{m}\times 5.5\ \mu\text{m}\times 165\ \text{nm}$ ), with one large electrode at one side and two small electrodes on the other side. Electrodes 2 and 3 are triangular and rectangular shaped, respectively. **f**,  $H_C$  as a function of DC current and the current path in device 3. **g**, The evolution of  $H_C$  given by the current-assisted DW motion model in the simple case where two nucleation sites with different DW nucleation field  $H_n$  located under source and drain electrodes.  $H_n$  at the two sites are colored red and blue, respectively, and the smallest  $H_n$  determines the coercive field (solid line). When the current reaches the value marked by the purple arrow, where  $H_{n,1}=H_{n,2}$ , the decisive nucleation site changes (also shown in **d**). All data in **Fig. 2** are measured at 150 K.

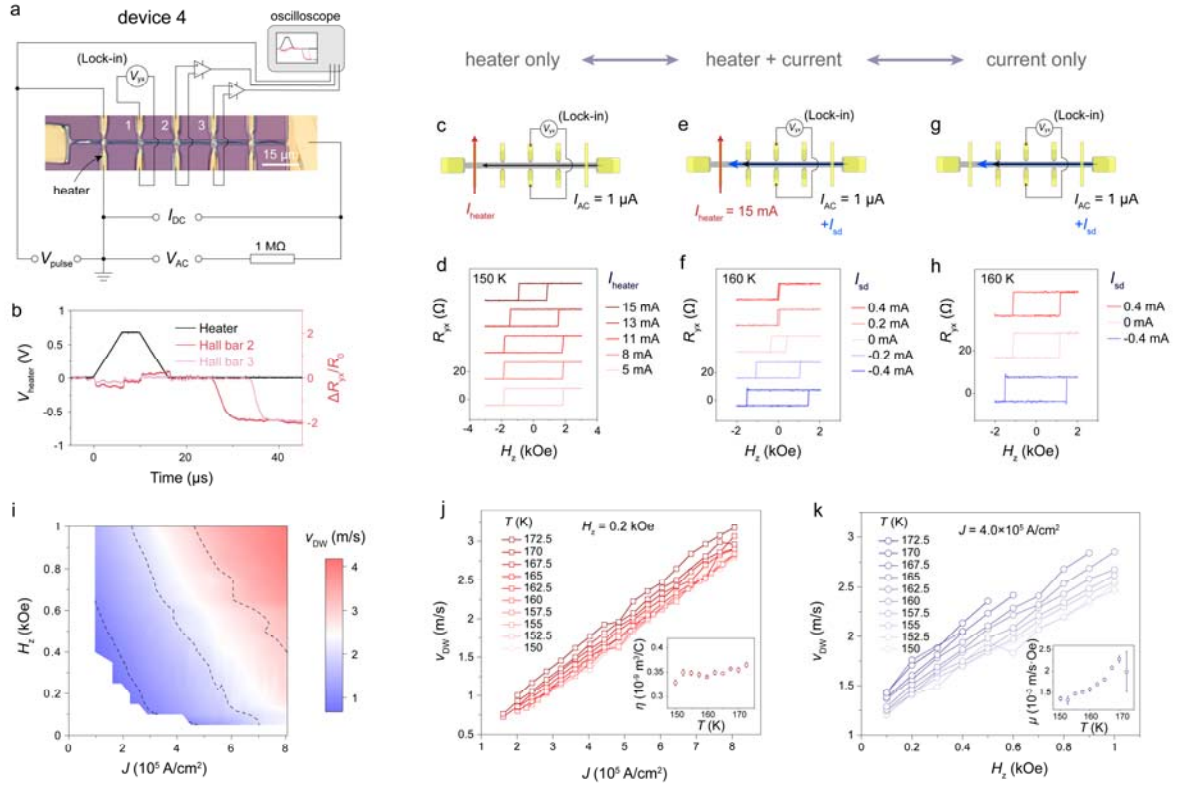


**Fig. 3 Domain wall velocity measurement.** **a**, Schematic diagram of the domain wall velocity measurement and optical image of the tested nanowire device (device 4,  $90 \mu m \times 1 \mu m \times 62 nm$ ). The Hall voltage signals are transmitted to the oscilloscope through  $1000\times$  gain preamplifiers. **b**, Typical waveform obtained during a measurement. Black line shows the voltage pulse applied onto the heater. Red lines trace the change of  $R_{yx}$ . Domain wall velocity  $v_{DW}$  equals the channel length between the two Hall bars divided by the time interval of  $R_{yx}$  reversal. **c-h**, Control experiments to separate the contribution of Joule heating (by  $I_{heater}$ ) and STT (by  $I_{sd}$ ) in the magnetism modulation process. The  $R_{yx}$  hysteresis loops are measured through  $1 \mu A$  AC current that minimizes its influence on magnetization reversal. **i**, Contour map of  $v_{DW}$  as a function of out-of-plane field  $H_z$  and current density  $J$ . Black dashed lines show “iso-speed” lines with a spacing of 1 m/s. **j**,  $v_{DW}$  as a function of  $J$  and  $T$ , measured under  $H_z = 0.2 kOe$ . Inset, the current-dependent DW mobility  $\eta$  as a function of  $T$ . **k**,  $v_{DW}$  as a function of  $H_z$  and  $T$ , measured at  $J = 4.0 \times 10^5 A/cm^2$ . Inset, the field-dependent DW mobility  $\mu$  as a function of  $T$ .

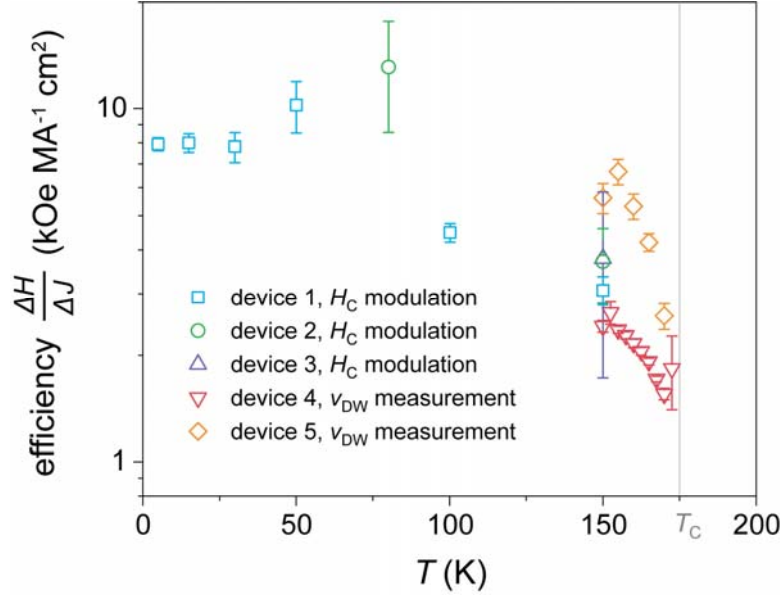


**Fig. 4 The STT efficiency  $\Delta H/\Delta J$  given by two independent methods.** As described in the main text, devices 1-3 are Hall-bar devices, and the efficiency is given by the current modulation process of coercive field  $H_C$ , which is  $\Delta H_C/\Delta J$ . Device 4-5 are nanowire devices, and the efficiency is given by the current-induced effective field in DW velocity measurements, which is  $\Delta H/\Delta J = \eta/\mu$  [ $\eta(\mu)$ , current(field)-dependent DW mobility]. These data from different devices and methods show good consistency, providing strong evidence of the giant STT efficiency in  $\text{Co}_3\text{Sn}_2\text{S}_2$ .

## Methods

**Sample Growth and Device Fabrication**  $\text{Co}_3\text{Sn}_2\text{S}_2$  nanoflakes are grown on sapphire or Si/SiO<sub>2</sub> substrates via a modified chemical vapor transport method.  $\text{Co}_3\text{Sn}_2\text{S}_2$  powders are sealed in one end of an ampule as precursors with transport agents, and substrates are placed at the other end (see Supplementary Fig. S1). To reduce the transport rate, a neck of a diameter of 1 mm is introduced in the middle of the ampule. The source and the sink ends are gradually heated to 1000 °C and 800 °C in 3 hours, and the temperatures are kept for 1 hour. After natural cooling to room temperature, high-quality crystals are obtained, confirmed by high resolution transmission electron microscope and selected area electron diffraction patterns. The thicknesses of the samples are measured by atomic force microscopy. The nanoflakes are patterned into designed geometry by electron beam lithography and argon ion milling. After that, Cr/Au (10 nm/100 nm) electrodes are defined by electron beam lithography and evaporation.

**Transport Measurement** The device is loaded into a PPMS (Cryomagnetics, Inc.) with a magnetic field up to 14 T. For all-DC measurements (which is the case for devices 1-3), the current is applied by Keithley 2636B. Longitudinal and transverse voltage are measured by Keithley 2636B and 2182A, respectively. The devices show linear  $I$ - $V$  curves in the measured current range, so the resistance can be directly obtained by dividing the voltage by the DC current. A small current of 100  $\mu\text{A}$  is used to obtain the  $R$ - $T$  and  $H_c$ - $\theta$  data. A self-made rotator probe is used for angular-dependent measurements. For current modulation measurements, the hysteresis loops can be obtained by directly sweeping the magnetic field or by holding the field but rotating the sample.

**Domain Wall Velocity Measurement** The schematic diagram to measure the DW velocity is shown in Fig. 3a. The AC signal is applied and measured by SR830 lock-in amplifier. The DC current is applied by Keithley 2636B. The current pulse is generated by AFG31000 arbitrary function generator. The Hall voltage signal is magnified 1000 $\times$  by Signal Recovery 5186 preamplifier and is then traced by DPO2024B oscilloscope. The pulse duration on the heater is set to 10  $\mu\text{s}$  to ensure DW generation, with rise/fall time set to be 5  $\mu\text{s}$  to minimize interference on the Hall signal. As a result, clean jump signals are obtained when DW passes the Hall bar. Background signals are filtered by a 0.5 Hz cut-off frequency of the preamplifier.

### Data availability

The datasets generated by the present study are available from the corresponding author upon request.

### Acknowledgements

The authors thank L. Liu and Y. Zhu for valuable discussions, X. Cheng for RMCD measurements, and J. Zhang for MFM measurements. This work was supported by the National Key R&D Program of China (Grant Nos. 2017YFA0206301, 2018YFA0306900 and 2019YFA0704900), the National Natural Science Foundation of China (Grant Nos. 6152004, 11974394, 51631001 and 51672010), and the Strategic Priority Research Program (B) of the Chinese Academy of Sciences (XDB33000000).

### Author contributions

Q.W. and Y.Y. conceived the project. Y.Z. grew the  $\text{Co}_3\text{Sn}_2\text{S}_2$  nanoflakes and fabricated the devices assisted by K.Y.. Q.Z. and E.L. provided the precursor  $\text{Co}_3\text{Sn}_2\text{S}_2$  powders and helpful discussion of preparing the nanoflake samples. Q.W. conducted the transport measurements assisted by Y.Z., K.Y., and P.G.. Q.W. analyzed the data. X.X. performed HRTEM measurements. E.L. and K.N. provided scientific discussions. Q.W. and Y.Y. wrote the manuscript, with input from all authors. Y.H. and Y.Y. supervised the project. All authors discussed the results, interpretation and conclusion.

### Competing interests

The authors have filed a Chinese patent application for using direct current injection to modulate magnetism in magnetic semimetal thin films.

### References

1. Myers, E. B. Current-Induced Switching of Domains in Magnetic Multilayer Devices. *Science* **285**, 867–870 (1999).
2. Parkin, S. S. P., Hayashi, M. & Thomas, L. Magnetic Domain-Wall Racetrack Memory. *Science* **320**, 190–194 (2008).
3. Luo, Z. *et al.* Current-driven magnetic domain-wall logic. *Nature* **579**, 214–218 (2020).
4. Raymenants, E. *et al.* Nanoscale domain wall devices with magnetic tunnel junction read and write. *Nat Electron* **4**, 392–398 (2021).
5. Berger, L. Exchange interaction between ferromagnetic domain wall and electric current in very thin metallic films. *Journal of Applied Physics* **55**, 1954–1956 (1984).
6. Tatara, G. & Kohno, H. Theory of Current-Driven Domain Wall Motion: Spin Transfer versus Momentum Transfer. *Phys. Rev. Lett.* **92**, 086601 (2004).
7. Zhang, S. & Li, Z. Roles of Nonequilibrium Conduction Electrons on the Magnetization Dynamics of Ferromagnets. *Phys. Rev. Lett.* **93**, 127204 (2004).
8. Tatara, G., Kohno, H. & Shibata, J. Microscopic approach to current-driven domain wall dynamics. *Physics Reports* **468**, 213–301 (2008).
9. Miron, I. M. *et al.* Perpendicular switching of a single ferromagnetic layer induced by in-plane current injection. *Nature* **476**, 189–193 (2011).
10. Liu, L., Lee, O. J., Gudmundsen, T. J., Ralph, D. C. & Buhrman, R. A. Current-Induced Switching of Perpendicularly Magnetized Magnetic Layers Using Spin Torque from the Spin Hall Effect. *Phys. Rev. Lett.* **109**, 096602 (2012).

11. Liu, L. *et al.* Spin-Torque Switching with the Giant Spin Hall Effect of Tantalum. *Science* **336**, 555–558 (2012).
12. Khang, N. H. D., Ueda, Y. & Hai, P. N. A conductive topological insulator with large spin Hall effect for ultralow power spin–orbit torque switching. *Nature Mater* **17**, 808–813 (2018).
13. Dc, M. *et al.* Room-temperature high spin–orbit torque due to quantum confinement in sputtered BixSe(1–x) films. *Nature Mater* **17**, 800–807 (2018).
14. Yamaguchi, A. *et al.* Real-Space Observation of Current-Driven Domain Wall Motion in Submicron Magnetic Wires. *Phys. Rev. Lett.* **92**, 077205 (2004).
15. Feigenson, M., Reiner, J. W. & Klein, L. Efficient current-induced domain-wall displacement in SrRuO<sub>3</sub>. *Physical review letters* **98**, 247204 (2007).
16. Koyama, T. *et al.* Current-induced magnetic domain wall motion below intrinsic threshold triggered by Walker breakdown. *Nature Nanotech* **7**, 635–639 (2012).
17. Gushi, T. *et al.* Large Current Driven Domain Wall Mobility and Gate Tuning of Coercivity in Ferrimagnetic Mn<sub>4</sub>N Thin Films. *Nano Lett.* **19**, 8716–8723 (2019).
18. Yamanouchi, M., Chiba, D., Matsukura, F. & Ohno, H. Current-induced domain-wall switching in a ferromagnetic semiconductor structure. *Nature* **428**, 539–542 (2004).
19. Yamanouchi, M. *et al.* Universality Classes for Domain Wall Motion in the Ferromagnetic Semiconductor (Ga,Mn)As. *Science* **317**, 1726–1729 (2007).
20. Liu, L. *et al.* Electrical switching of perpendicular magnetization in a single ferromagnetic layer. *Phys. Rev. B* **101**, 220402 (2020).
21. Zhang, K. *et al.* Gigantic Current Control of Coercive Field and Magnetic Memory Based on Nanometer-Thin Ferromagnetic van der Waals Fe<sub>3</sub>GeTe<sub>2</sub>. *Adv. Mater.* **33**, 2004110 (2021).
22. Kurebayashi, D. & Nomura, K. Theory for spin torque in Weyl semimetal with magnetic texture. *Sci Rep* **9**, 5365 (2019).
23. Kurebayashi, D., Araki, Y. & Nomura, K. Microscopic Theory of Electrically Induced Spin Torques in Magnetic Weyl Semimetals. *J. Phys. Soc. Jpn.* **90**, 084702 (2021).
24. Belopolski, I. *et al.* Discovery of topological Weyl fermion lines and drumhead surface states in a room temperature magnet. *Science* **365**, 1278–1281 (2019).
25. Li, P. *et al.* Giant room temperature anomalous Hall effect and tunable topology in a ferromagnetic topological semimetal Co<sub>2</sub>MnAl. *Nat Commun* **11**, 3476 (2020).
26. Liu, E. *et al.* Giant anomalous Hall effect in a ferromagnetic kagome-lattice semimetal. *Nature physics* **14**, 1125–1131 (2018).
27. Wang, Q. *et al.* Large intrinsic anomalous Hall effect in half-metallic ferromagnet Co<sub>3</sub>Sn<sub>2</sub>S<sub>2</sub> with magnetic Weyl fermions. *Nat Commun* **9**, 3681 (2018).
28. Liu, D. F. *et al.* Magnetic Weyl semimetal phase in a Kagomé crystal. *Science* **365**, 1282–1285 (2019).
29. Morali, N. *et al.* Fermi-arc diversity on surface terminations of the magnetic Weyl semimetal Co<sub>3</sub>Sn<sub>2</sub>S<sub>2</sub>. *Science* **365**, 1286–1291 (2019).
30. Tanaka, M. *et al.* Topological Kagome Magnet Co<sub>3</sub>Sn<sub>2</sub>S<sub>2</sub> Thin Flakes with High Electron Mobility and Large Anomalous Hall Effect. *Nano Lett.* **20**, 7476–7481 (2020).
31. Shen, J. *et al.* On the anisotropies of magnetization and electronic transport of magnetic Weyl semimetal Co<sub>3</sub>Sn<sub>2</sub>S<sub>2</sub>. *Appl. Phys. Lett.* **115**, 212403 (2019).

32. Metaxas, P. J. *et al.* Creep and Flow Regimes of Magnetic Domain-Wall Motion in Ultrathin Pt / Co / Pt Films with Perpendicular Anisotropy. *Phys. Rev. Lett.* **99**, 217208 (2007).
33. Mougín, A., Cormier, M., Adam, J. P., Metaxas, P. J. & Ferré, J. Domain wall mobility, stability and Walker breakdown in magnetic nanowires. *Europhys. Lett.* **78**, 57007 (2007).
34. Beach, G. S. D., Tsoi, M. & Erskine, J. L. Current-induced domain wall motion. *Journal of Magnetism and Magnetic Materials* **320**, 1272–1281 (2008).
35. Díaz Pardo, R. *et al.* Common universal behavior of magnetic domain walls driven by spin-polarized electrical current and magnetic field. *Phys. Rev. B* **100**, 184420 (2019).
36. Lee, J.-C. *et al.* Universality Classes of Magnetic Domain Wall Motion. *Phys. Rev. Lett.* **107**, 067201 (2011).
37. A mechanism of magnetic hysteresis in heterogeneous alloys. *Phil. Trans. R. Soc. Lond. A* **240**, 599–642 (1948).
38. Cullity, B. D. & Graham, C. D. *Introduction to magnetic materials*. (2015).
39. Thiaville, A. & Nakatani, Y. Domain-Wall Dynamics in Nanowires and Nanostrips. in *Spin Dynamics in Confined Magnetic Structures III* (eds. Hillebrands, B. & Thiaville, A.) vol. 101 161–205 (Springer Berlin Heidelberg, 2006).
40. Manchon, A. *et al.* Current-induced spin-orbit torques in ferromagnetic and antiferromagnetic systems. *Rev. Mod. Phys.* **91**, 035004 (2019).
41. Yoshimura, Y. *et al.* Soliton-like magnetic domain wall motion induced by the interfacial Dzyaloshinskii–Moriya interaction. *Nature Phys* **12**, 157–161 (2016).
42. Kim, K.-J. *et al.* Fast domain wall motion in the vicinity of the angular momentum compensation temperature of ferrimagnets. *Nature Mater* **16**, 1187–1192 (2017).
43. Ilan, R., Grushin, A. G. & Pikulin, D. I. Pseudo-electromagnetic fields in 3D topological semimetals. *Nat Rev Phys* **2**, 29–41 (2020).
44. Araki, Y. Magnetic Textures and Dynamics in Magnetic Weyl Semimetals. *ANNALEN DER PHYSIK* **532**, 1900287 (2020).